

# The internal consistency, stability, and accuracy of the discrete, compatible formulation of Lagrangian hydrodynamics

A.L. Bauer<sup>a,b,\*</sup>, D.E. Burton<sup>c</sup>, E.J. Caramana<sup>d</sup>, R. Loubère<sup>e</sup>,  
M.J. Shashkov<sup>b</sup>, P.P. Whalen<sup>f</sup>

<sup>a</sup> *Department of Mathematics, University of Michigan, 2074 East Hall, 530 Church Street, Ann Arbor, MI 48109-1043, USA*

<sup>b</sup> *T-7, MS B284, Los Alamos National Laboratory, Los Alamos, NM, USA*

<sup>c</sup> *X-3, MS T086, Los Alamos National Laboratory, Los Alamos, NM, USA*

<sup>d</sup> *CCS-2, MS D413, Los Alamos National Laboratory, Los Alamos, NM, USA*

<sup>e</sup> *MIP, University of Toulouse, 31062 Toulouse Cedex 9, France*

<sup>f</sup> *X-7, MS F644, Los Alamos National Laboratory, Los Alamos, NM, USA*

Received 30 November 2005; received in revised form 21 February 2006; accepted 23 February 2006

Available online 19 April 2006

## Abstract

This work explores the somewhat subtle meaning and consequences of the salient properties of the discrete, compatible formulation of Lagrangian hydrodynamics. In particular, since this formulation preserves total energy to roundoff error, the amount of error in the conservation of total energy cannot be used to gauge the internal consistency of calculations, as is often done with the older forms of this algorithm. However, the compatible formulation utilizes two definitions of zone volume: the first is the usual definition whereby the volume of a zone is defined as some prescribed function of the coordinates of the points that define it; the second is given as the integration in time of the continuity equation for zone volume as expressed in Lagrangian form. It is the use of this latter volume in the specific internal energy equation that enables total energy to be exactly conserved. These two volume definitions are generally not precisely equal. It is the analysis of this difference that forms the first part of this study. It is shown that this difference in zone volumes can be used to construct a practical internal consistency measure that not only takes the place of the lack of total energy conservation of the older forms of Lagrangian hydrodynamics, but is more general in that it can be defined on a single zone basis. It can also be used to ascertain the underlying spatial and temporal order of accuracy of any given set of calculations. The difference in these two definitions of zone volume may be interpreted as a type of entropy error. However, this entropy error is found to be significant only when a given calculation becomes numerically unstable, otherwise it remains at or far beneath truncation error levels. In fact, it can be utilized to provide an upper bound on the size of the spatial truncation error for a stable computation. It is also shown how this volume difference can be used as an indicator of numerical difficulties, since exact local conservation of total energy does not guarantee numerical stability or the quality of any numerical calculation. The discrete, compatible formulation of Lagrangian hydrodynamics utilizes a two level predictor/corrector-type of time integration scheme; a stability analysis, both analytical and numerical, is given. This analysis reveals a novel stability diagram

\* Corresponding author. Tel.: +1 734 936 4557/997 0509; fax: +1 734 763 0937.

E-mail addresses: [albauer@umich.edu](mailto:albauer@umich.edu) (A.L. Bauer), [burton@lanl.gov](mailto:burton@lanl.gov) (D.E. Burton), [ed.caramana@gmail.com](mailto:ed.caramana@gmail.com) (E.J. Caramana), [loubere@mip.ups-tlse.fr](mailto:loubere@mip.ups-tlse.fr) (R. Loubère), [shashkov@lanl.gov](mailto:shashkov@lanl.gov) (M.J. Shashkov), [ppw@lanl.gov](mailto:ppw@lanl.gov) (P.P. Whalen).

that has not been heretofore published, and gives definitive information as to how the stabilizing corrector step should be centered in time.

© 2006 Elsevier Inc. All rights reserved.

*Keywords:* Lagrangian scheme; Stability; Compressible fluids; Compatible discretization; Support operator

## 1. Introduction

The Lagrangian formulation of the equations of hydrodynamics has a very old and venerable history. Indeed, the very first large-scale numerical calculations that resemble modern computer simulations in both complexity and in the numerical issues considered utilized fluid equations in the Lagrangian frame of reference in one-dimension [1]. If one considers an arbitrary fluid velocity  $v$  and distinct sound speed  $c_s$ , then in one-dimension the characteristic trajectories of the fluid equations have associated eigenvalues  $v \pm c_s$  and  $v$ . In the Lagrangian frame that follows the fluid velocity  $v$ , these eigenvalues transform into the Galilean invariant values  $\Delta v \pm c_s$  and  $\Delta v$ , where  $\Delta v$  is the difference in velocity between two adjacent discrete spatial locations in the flow field. Thus, the Lagrangian frame of reference is unique, and one characteristic is chosen and followed exactly, except for spatial gradients in the velocity field. The fact that the Lagrangian description of fluid dynamics is automatically adaptive makes it the preferred representation in one-dimension. Newton's second law of motion,  $\vec{F} = M\vec{a}$ , where  $M$  is the mass of a point particle (or fluid element),  $\vec{F}$  is the total force acting on it, with the acceleration  $\vec{a}$  given as the second derivative with respect to time of its displacement vector  $\vec{r}$ , is a statement set in the Lagrangian frame of reference. Discretizing this equation directly with respect to time utilizing  $\vec{r}$  as a dependent variable results quite naturally in the three-level leapfrog scheme. These time levels are usually denoted as  $n - 1$ ,  $n$ , and  $n + 1$ , with the force  $\vec{F}$  spatially differenced in some manner but placed at time level  $n$ . All early Lagrangian algorithms in both 1D [2] and in 2D [3] utilized this kind of discretization with respect to time. Although this forms a simple and intuitive numerical integration scheme, it leaves the velocity of a mass point or fluid element defined only as the difference between its displacement vector at two different time levels, and therefore the velocity is defined only at the  $n \pm \frac{1}{2}$  time levels. When one then considers the total energy of a fluid as a sum of both kinetic energy and internal energy that can be exchanged between each other by the action of forces, this sum is difficult to conserve exactly in discrete form owing to the fact that the two components that comprise it are defined at different time levels. When velocity dependent forces are explicitly added to this model, as with the artificial viscosity [4], this type of time integration becomes somewhat clumsy and looks even contrived [2], since the artificial viscosity terms must be lagged in time to preserve numerical stability.

The spatial discretization of the force in all early versions of Lagrangian hydrodynamics [2,3] is some form of what is presently known as finite-volume differencing. That is, these various forms calculate force as a stress (scalar pressure plus deviators) times a normal surface-area vector. The most modern of these older force calculations is the diamond differencing scheme due to Wilkins [3], which uses closed surface area contours to calculate the force acting on a point, and thus properly conserves linear momentum in a trivial manner. Others piece the force contributions together in various ways to form the total force acting on each fluid element such that strict conservation of linear momentum may, or may not, be obtained. Most Lagrangian hydrodynamics codes employ a spatially staggered placement of dependent variables with stress, density, and specific internal energy given in zones surrounded by points that have associated position and velocity vectors. This enables the calculation of forces by means of the various kinds of finite-volume differencing referenced above, with masses and volumes ascribed to both zones and points in an interleaved manner. This also avoids the "grid-decoupling" instability that is the bane of non-staggered forms of this algorithm. A difficulty with the older work is that there was no agreement amongst the various authors of these different algorithms as to how these schemes, aside from the noted common features, should be constructed. The choices made were largely arbitrary and not tied to solid mathematical concepts.

An early attempt to remedy this lack of a sound theoretical basis is the work of Goad [5], who used the method of virtual work to derive a form of finite-volume force differencing of the stress in 2D cylindrical

geometry. This work was little noted, partly because this type of scheme does not yield the limit of 1D spherical geometry from 2D cylindrical geometry that is important in some applications [6]. Next, finite element spatial discretizations were utilized. However, these must be of low order accuracy to prevent the occurrence of non-physical oscillations about shock discontinuities that appear if the support of the basis functions is too large. Thus, finite element spatial representations only give the appearance of a rigorous foundation while sacrificing the flexibility that a finite-volume discretization affords.

The work that first places this type of finite-volume algorithm on a firm theoretical basis is that of Favorskii [7], and independently, Margolin and Adams [8]. The first paper shows that the discrete equations in Lagrangian form can be generally derived from a variational principle. It also justifies the use of the surface area vectors of closed volumes as proper discretization objects, a practice that was previously employed, but not always correctly, in that the surface areas about a point did not in all cases sum to zero. The second paper parallels this work. Its central thrust is to use the continuity equation in discrete form to derive finite-volume differencing given a discrete expression for the volume of a zone. This again results in, and justifies, the surface areas utilized to calculate the force employed. It emphasizes that the difference formulas that are derived are “operator” expressions that can be used to calculate discrete derivatives of any function, and not just of the velocity field that they originally act upon. It is the discrete form of the continuity equation as emphasized in [8] that is central to our discussion of internal consistency. A further extension of the work of Favorskii results in what has become known as the “method of support operators” [9]. Although this work is more general than just its application to the equations of Lagrangian hydrodynamics, it is this system of equations that is used in its original exposition. This method also utilizes the continuity equation in discrete form to derive the divergence “operator” and then uses the vector identities in summation form to derive discrete versions of all other operators. It emphasizes the relation in discrete form of the divergence and gradient operators as negative adjoints of each other as in the continuum case. The paper of Margolin and Tarwater [10] again parallels this work. It derives the gradient operator from the divergence operator by using the same requirement – that they must be negative adjoints. This is done in the context of deriving a compatible expression for the diffusion operator as the direct product of gradient and divergence, and requires additionally that this diffusion operator be exact for a linear function. These publications all revolve around the central idea that the discrete equations must obey the global properties of the continuum ones in order to be considered as valid discretizations that will then mirror continuum conservation properties in their discrete analogs. They thus remove the arbitrary and heuristic formulations of the previous, but well-used, codes based on the older work [3].

Somewhat after the previously cited developments is the seminal work of Burton [11,12], which discretizes the fluid equations in Lagrangian form on a staggered spatial grid utilizing subgrid quantities termed corner masses and corner forces, from which the zone and point masses, and the total force acting on a point, are constructed. A two-level time integration scheme is also utilized so that both kinetic energy and internal energy are defined at the same time level. The basic reasoning used by Burton to demonstrate conservation of total energy is the same as that employed in the method of support operators [9], and thus incorporates the important features of the previous works [8–10]. However, Burton’s formulation is more general in that he does not consider forces, or differential operators, of any specific origin. Instead, he utilizes an arbitrary corner force that allows the specification of forces of any functional form, with the work that they perform completely defined and total energy exactly conserved. The only restriction on the discrete form of the corner force is the relatively mild physical constraint of momentum conservation. He also notes [12] that this formulation of the Lagrangian hydrodynamics equations contains two distinct definitions of zone volume, and considers this difference to be a form of “entropy” error.

It is this latter work of Burton that we refer to herein as the “discrete, compatible formulation of Lagrangian hydrodynamics”, and which was initially constructed on arbitrary polyhedral grids [12]. The word “discrete” has been inserted to emphasize that these equations are essentially created in discrete form, as opposed to being the discretization of a system of PDE’s. As such, one may or may not be able to rigorously take the continuum limit to obtain the latter; this depends on the kinds of forces that are employed to resolve shocks and to counteract spurious grid motions. It is the subject of this paper to explore important consequences of this formulation. To this end a very brief statement of it is given that includes the definition of the two zone volumes that are central to investigating its internal consistency. A study of this novel internal

consistency feature is then developed theoretically and illustrated with numerical examples. A stability analysis of the time integration scheme utilized follows; last, our principal conclusions are briefly summarized.

### 2. Discrete, compatible Lagrangian hydrodynamics

Since the numerical algorithm that we term the discrete, compatible formulation of Lagrangian hydrodynamics has been given elsewhere [12,13], we repeat only that skeleton portion that is necessary to explore the features of it that are the subject of this work. To this end, consider the momentum equation given in discrete form as

$$M_p(\vec{v}_p^{n+1} - \vec{v}_p^n) = \sum_z \vec{f}_z^{p,*} \Delta t \equiv \vec{F}_p^* \Delta t. \tag{2.1}$$

To define the terms that occur in this equation we make reference to Fig. 1. This shows a small section of a quadrilateral grid in 2D Cartesian geometry with a single zone labelled by the integer index  $z$ , and with its four defining points labelled by the integer index  $p$ ; these indices range over all zones and points in the computational domain, respectively. Unique to each zone and each point, considered together as a pair-object, is a corner mass  $m_z^p$  and a corner force  $\vec{f}_z^p$ . The indices of these objects are placed so that the lower one is always summed with the upper one fixed; the asterisk used as a superscript on the force in Eq. (2.1) denotes time-centering, an issue discussed further on. The point mass  $M_p$  is formed by summing all  $m_z^p$ 's that have the same index  $p$ , where a particular  $m_z^p$  corresponds to the grey region in Fig. 1; likewise, the zone mass  $M_z$  that enters Eq. (2.2), is defined as the sum of all  $m_z^p$  that have the same zone index  $z$ . On this staggered spatial grid the points  $p$  carry a velocity  $\vec{v}_p$  that, when multiplied by the point mass  $M_p$ , represents an average momentum over the median mesh volume, depicted in Fig. 1 as the closed, dashed curve. The position vector  $\vec{r}_p$  of the point  $p$  is advanced from time level  $n$  to time level  $n + 1$  in a timestep  $\Delta t$  as,  $\Delta \vec{r}_p \equiv (\vec{r}_p^{n+1} - \vec{r}_p^n) = (\vec{v}_p^{n+1} + \vec{v}_p^n) \Delta t / 2$ , a form that is unique [14]. As is seen in Eq. (2.1) the total force  $\vec{F}_p^*$  that acts on mass  $M_p$  is made up of the sum of all corner forces  $\vec{f}_z^{p,*}$  with common point index  $p$ . The corner force  $\vec{f}_z^{p,*}$  mediates the exchange of kinetic energy and internal energy between a zone  $z$  and a point  $p$ ; its construction is at this stage completely general.

The most important result of this hydrodynamics formulation, and that which is termed ‘‘compatible’’, is that if at any time  $t^n$  a definition of total energy is given as,  $E_T(t^n) \equiv \frac{1}{2} \sum_p M_p (\vec{v}_p^n)^2 + \sum_z M_z e_z^n$ , then in conjunction with the momentum equation, Eq. (2.1), an equation in discrete form for the evolution of the specific internal energy  $e_z$ , defined in the zones  $z$ , results and is given as

$$M_z(e_z^{n+1} - e_z^n) \equiv - \sum_p \vec{f}_p^{z,*} \cdot \Delta \vec{r}_p. \tag{2.2}$$

In Eq. (2.2) the corner force  $\vec{f}_p^{z,*}$  is the same as that used in the momentum equation above except that it is now summed with respect to fixed zone index  $z$ ; all other quantities in Eq. (2.2) have been defined. As noted in

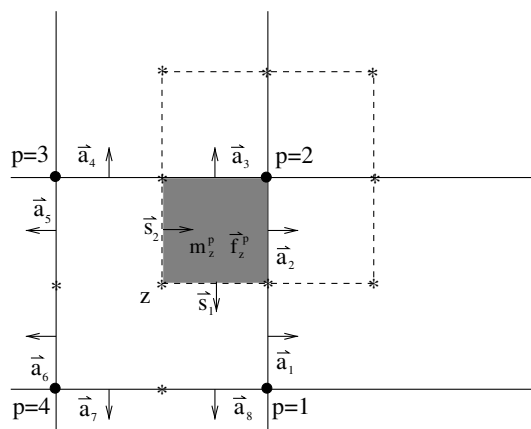


Fig. 1. Notation for a given quadrilateral zone  $z$  (solid line) with points  $p = 1, 2, 3, 4$ . The median mesh is drawn with a dashed line.  $\vec{s}_1, \vec{s}_2$  are the median mesh vectors. The grey region is a corner subcell whose associated mass and force are  $m_z^p$  and  $\vec{f}_z^p$ , respectively.

previous work [13,14], this formulation of Lagrangian hydrodynamics consists of three discrete equations: momentum, specific internal energy, and total energy, such that the specification of any two results in the third. These three equations form an algebraic identity. Also, as discussed previously [13,14], for these equations to make physical sense the arbitrary corner force  $\vec{f}_p^{z,*}$  must sum to zero in any zone  $z$ ; this represents Galilean invariance of the discrete equations.

The primary quantity that must be computed with this form of hydrodynamics to advance the dependent variables in time is the corner force. To advance a timestep  $\Delta t$  this force is first calculated at the  $n$  time level where all quantities are known; the dependent variables are then advanced to the  $n + 1$  time level. However, to obtain numerical stability, as discussed in Section 4, this cycle is repeated with the corner forces recalculated at some time level between half-forward or time centered ( $* = n + \frac{1}{2}$ ), and full-forward ( $* = n + 1$ ). The exact functional form of the corner forces can be quite complicated, and is not at all unique. This has been discussed in depth elsewhere [6,12,14–17]. Here we are concerned with Eq. (2.2) for pressure forces, and how it represents a discrete form of what is generally known as  $P dV$  work; that is, how does this equation calculate the work done by a zone pressure  $P_z^*$  that is constant throughout the given zone  $z$ ? The work performed by the “generic” RHS of Eq. (2.2) can be written for pressure forces as:

$$-\sum_p \vec{f}_p^{z,*} \cdot \Delta \vec{r}_p \equiv -P_z^* (\Delta V)_z = -P_z^* V_z (\nabla \cdot \vec{v})_z \Delta t, \quad (2.3)$$

where  $(\Delta V)_z$  is the change in volume of zone  $z$  in timestep  $\Delta t$ . That this second term is equal to the third term in the above equation is a consequence of the continuity equation for volume in Lagrangian form. More explicitly, if we consider the equation of continuity for the zone density (where zone density  $\rho_z$  is defined as  $\rho_z \equiv M_z/V_z(t)$ ) as  $\partial \rho / \partial t + \nabla \cdot \rho \vec{v} = 0$ , then using the definition given for  $\rho_z$  one obtains

$$\frac{dV_z}{dt} = V_z (\nabla \cdot \vec{v})_z, \quad (2.4)$$

which in the “support operators” terminology [9] yields a “discrete” definition of  $(\nabla \cdot \vec{v})_z$ , or of the divergence operator. To see this, consider that the zone volume depends on some arbitrary number of coordinates  $d$  ( $p = 1, \dots, d$ ), so that  $V_z^n = V_z(\vec{r}_1^n, \dots, \vec{r}_d^n)$ ; putting this form into Eq. (2.4) results in

$$\frac{dV_z}{dt} = \sum_{p=1}^d \sum_{i=1}^3 \frac{\partial V_z}{\partial x_{p,i}} v_{p,i} \equiv \sum_{p=1}^d \vec{\alpha}_p^z \cdot \vec{v}_p = V_z (\nabla \cdot \vec{v})_z, \quad (2.5)$$

where in the first part of this equation  $\vec{r}_p$  consists of the three Cartesian components  $x_{p,i}$ , and the velocity components  $v_{p,i}$  are defined by the fact that the points are Lagrangian,  $v_{p,i} \equiv dx_{p,i}/dt$ . The derivatives of the zone volume with respect to its coordinate dependence is used to define the surface vectors associated with point  $p$ , as was done in the work of Favorskii [7], and Margolin and Adams [8]. Thus the grid vectors used to construct the corner forces are not arbitrarily specified, as with the older versions of this type of hydrodynamics [3], but are a consequence of the chosen volume definitions. (One interesting case is area-weighted differencing, see [13].) Under this construction, we can write the equations for the grid vector and corner force associated with  $P dV$  work of point  $p$  and zone  $z$  as

$$\vec{\alpha}_{p,i}^z = \frac{\partial V_z}{\partial x_{p,i}}, \quad \vec{f}_z^p = P_z \vec{\alpha}_p^z. \quad (2.6)$$

Referring to the definitions illustrated in Fig. 1 for point  $p = 2$  of zone  $z$  we have that  $\vec{\alpha}_{p=2}^z = \vec{a}_2 + \vec{a}_3$ , where for the quadrilateral shown the  $\vec{a}_j$  vectors ( $j = 1, \dots, 8$ ) are outward normal to zone  $z$  with a magnitude of one-half of their respective edge length.

The preceding discussion justifies the claim that the work done by a zone pressure is a proper differencing of  $P dV$ . However, Eq. (2.2) calculates the work done by all zone forces of any origin. This is an important generalization when one needs to calculate the work done by the artificial stresses used with this kind of hydrodynamics. Defining the surface area vectors of a prescribed volume as given by the derivative of that volume with respect to coordinates is essentially a generalization of the result in elementary calculus where the derivative of the area of a circle, or of the volume of a sphere, yields its surface area to the case where the volume in question does not have a simply differentiable boundary.

That the use of two different definitions of zone volume results in what may be described as an entropy error can be seen by considering the first law of thermodynamics for a zone  $z$ , written as

$$M_z \Delta e_z = -P_z(\rho_z = M_z/V_z^{\text{crd}}; e_z) \Delta V_z^{\text{cmp}} + (T \Delta S)_z, \quad (2.7)$$

where  $S$  is the entropy and  $T$  is the temperature. In this equation the density dependence of the zone pressure is a function of the coordinate volume  $V_z^{\text{crd}}$ , while the  $P dV$  work term involves the change in compatible volume  $V_z^{\text{cmp}}$  on a timestep. The entropy term completes the equation, and for adiabatic flow will not be exactly zero unless  $V_z^{\text{crd}} = V_z^{\text{cmp}}$ . The magnitude and implications of this difference are explored in the next section. However, it will be shown that using  $V_z^{\text{cmp}}$  to compute the density in Eq. (2.7) is not a valid way to make this equation internally consistent.

What has been demonstrated is that the volume change utilized in the discrete version of the specific internal energy written in compatible form is not the change in volume deduced from the difference in a zone volume calculated from its coordinates at two different times; but rather, this change in zone volume is calculated from the discrete evolution in time of the continuity equation for volume, Eq. (2.5). These two definitions of zone volume are not generally equal. The zone volume that is computed directly from its coordinates is hereon referred to as the “coordinate volume”, while that computed from integrating Eq. (2.5) in time is termed the “compatible volume”. How these two volumes differ and the consequences of this difference are the subject of the next section.

### 3. Internal consistency and accuracy

Given the previous discussion, it is convenient for the analysis that follows to contrast the change in volume of a zone calculated from its coordinates at two different times to that of the increment in zone volume as calculated from the evolution equation for volume. To this end, the change in coordinate zone volume  $(\Delta V)_z^{\text{crd}}$  during a timestep, where the coordinates are incremented by an amount  $\Delta \vec{r}_p$  and  $p = 1, \dots, d$ , is defined as

$$(\Delta V)_z^{\text{crd}} \equiv V_z^{n+1} - V_z^n = V_z[(\vec{r}_1^n + \Delta \vec{r}_1) \cdots (\vec{r}_d^n + \Delta \vec{r}_d)] - V_z[\vec{r}_1^n \cdots \vec{r}_d^n]. \quad (3.1)$$

From the previous arguments, the change in compatible zone volume  $(\Delta V)_z^{\text{cmp}}$  is given by

$$(\Delta V)_z^{\text{cmp}} = \sum_{p=1}^d \vec{a}_p^{z,*} \cdot \Delta \vec{r}_p, \quad (3.2)$$

where the time centering of the surface vectors  $\vec{a}_p^{z,*}$  of a zone remains to be specified. Since we are interested in only the change in compatible zone volume on the final corrector step, these vectors are centered somewhere between time levels  $* = n + \frac{1}{2}$  and  $* = n + 1$ , and not at time level  $* = n$  as is the case for the predictor step. Note that the displacement vectors  $\Delta \vec{r}_p$  of the grid points are the same in both of these equations.

A global internal consistency criterion can be constructed from a knowledge of both the coordinate and compatible zone volumes at any given time. The coordinate zone volume,  $V_z^{\text{crd}}(t^n)$ , is always given as a known function of the coordinates; however, the compatible zone volume must be constructed as a diagnostic on each timestep. That is, to obtain  $V_z^{\text{cmp}}(t^n)$  the continuity equation (2.5) must be integrated with respect to time, and  $V_z^{\text{cmp}}(t^n)$  updated at the end of every timestep as an additional dependent variable. Thus we have that

$$V_z^{\text{cmp}}(t^n) = V_z^{\text{crd}}(t=0) + \sum_{k=1}^n (\Delta V)_{z,k}^{\text{cmp}}, \quad (3.3)$$

where the sum is over all timesteps  $k$  to time  $t^n$ . Given these volume definitions, two useful norms can be defined as

$$E_1(t^n) \equiv \left( \sum_{z=1}^{N_z} |V_z^{\text{crd}}(t^n) - V_z^{\text{cmp}}(t^n)| / V_z^{\text{crd}}(t^n) \right) / N_z, \quad (3.4)$$

$$E_{\text{max}}(t^n) \equiv \max_z |V_z^{\text{crd}}(t^n) - V_z^{\text{cmp}}(t^n)| / V_z^{\text{crd}}(t^n), \quad (3.5)$$

where the sum in the first equation above, and the max operation in the second, is over all  $N_z$  zones of the grid. The average norm  $E_1(t^n)$  and the max norm  $E_{\text{max}}(t^n)$  serve to measure different and complimentary properties

of a computation. Also note that the kernel,  $|V_z^{\text{crd}}(t^n) - V_z^{\text{cmp}}(t^n)|/V_z^{\text{crd}}(t^n)$ , of these two norms is the same and is defined for every zone  $z$ . These values can be contoured spatially at any given time to yield additional detailed information about any simulation.

Our discussion of the difference in these two volume definitions begins in one dimension. Consider a set of zones in 1D with a numerical index  $j$  that ranges over the entire domain, where a single zone  $z$  (with index  $j$ ) is defined by boundary points with index labels  $j$  and  $j + 1$  that lie to the left and right, respectively. Next the difference in these two volumes is considered in 1D Cartesian, cylindrical, and spherical geometry. The case of 1D Cartesian geometry is trivial in that, in this instance, the grid vectors  $\vec{a}_p^{z,*}$  are equal to unity and fixed in time. Thus both definitions of zone volume are exactly equal.

The first non-trivial case is 1D cylindrical geometry. Let the grid point coordinates be denoted as  $R_j$ , then for a zone with index  $z = j$  it follows from Eq. (3.1) that the change in coordinate volume in a timestep is given by

$$\Delta V_z^{\text{crd}} = \pi \left[ (R_{j+1}^{n+1})^2 - (R_j^{n+1})^2 - (R_{j+1}^n)^2 + (R_j^n)^2 \right] = 2\pi \left[ R_{j+1}^n \Delta R_{j+1} + (\Delta R_{j+1})^2/2 - R_j^n \Delta R_j - (\Delta R_j)^2/2 \right], \quad (3.6)$$

where we have used the fact that  $R_j^{n+1} = R_j^n + \Delta R_j$ . To compute the corresponding compatible volume using Eq. (3.2), we specify the grid vectors as  $\vec{a}_{p=j}^{z,*} = 2\pi R_j^* = 2\pi(R_j^n + \alpha \Delta R_j^*)$ , where  $\Delta R_j^*$  is the displacement of point  $j$  from the predictor step, and  $0 \leq \alpha \leq 1$ . This yields the result

$$\Delta V_z^{\text{cmp}} = \vec{a}_{j+1}^{z,*} \Delta R_{j+1} - \vec{a}_j^{z,*} \Delta R_j = 2\pi \left[ (R_{j+1}^n \Delta R_{j+1} - R_j^n \Delta R_j) + \alpha (\Delta R_{j+1}^* \Delta R_{j+1} - \Delta R_j^* \Delta R_j) \right]. \quad (3.7)$$

By inspection these two equations are equal only if  $\alpha = 1/2$  and  $\Delta R_j^* = \Delta R_j$  for all points  $j$ . The first condition says that the grid vectors should be time-centered on the corrector step; the second is more severe and requires that the forces be exactly equal on both the predictor and corrector steps of a timestep cycle. This latter requirement is only true if the force is zero, since roundoff error in the calculation of the force will prevent this equality from holding in the case of non-zero forces.

If 1D spherical geometry is considered with the volume of a spherical zone given by  $4\pi(R_{j+1}^3 - R_j^3)/3$ , and with time-centered grid vectors  $\vec{a}_j^{z,*} = 4\pi(R_j^n + \Delta R_j^*/2)^2$ , then repeating the calculation given above one finds that the change in these volumes is also not identical; their difference is given by

$$\Delta V_z^{\text{crd}} - \Delta V_z^{\text{cmp}} = -4\pi \left[ \Delta R_{j+1} ((\Delta R_{j+1}^*)^2/4 - (\Delta R_{j+1})^2/3) - \Delta R_j ((\Delta R_j^*)^2/4 - (\Delta R_j)^2/3) \right]. \quad (3.8)$$

This difference is seen to arise from terms that are cubic in  $\Delta R_j$ . In the case of 1D spherical geometry, this defect can be remedied by a direct decomposition of the volume change of a spherical zone between time levels  $n$  and  $n + 1$  to yield an alternative form for the grid vectors in Eq. (3.8) as

$$\vec{a}_j^{z,*} = 4\pi[(R_j^{n+1,*})^2 + R_j^{n+1,*} R_j^n + (R_j^n)^2]/3. \quad (3.9)$$

In the above equation,  $R_j^{n+1,*}$  is the value of the coordinate of grid point  $j$  at the end of the predictor step,  $R_j^{n+1,*} = R_j^n + \Delta R_j^*$ . So if  $\Delta R_j^* = \Delta R_j$ , then  $R_j^{n+1,*} = R_j^{n+1}$  and the compatible volume calculated by using the grid vectors defined in Eq. (3.9) exactly matches the coordinate volume. The type of truncation error manipulation involved in the derivation of Eq. (3.9) cannot always be effected in the multi-dimensional case. The fact that coordinate and compatible volume definitions are not always equal for uniform drift is not a real defect with compatible Lagrangian hydrodynamics since, as will be shown, this difference remains at very small values, and both volumes are by themselves exactly conserved.

Next we continue our comparison of coordinate and compatible volume definitions by considering the case of 2D Cartesian geometry with quadrilateral zones. For coordinates  $\vec{r}_p^n$ , the volume of a quadrilateral using the notation of Fig. 1 is  $(\vec{r}_2 - \vec{r}_4) \times (\vec{r}_3 - \vec{r}_1)$ . From Eq. (3.1) this results in

$$\begin{aligned} \Delta V_z^{\text{crd}} &\equiv V_{\text{crd}}^{n+1} - V_{\text{crd}}^n \\ &= \frac{1}{2} [(\vec{r}_2 - \vec{r}_4)^n \times \Delta \vec{r}_3 + (\vec{r}_4 - \vec{r}_2)^n \times \Delta \vec{r}_1 + (\vec{r}_3 - \vec{r}_1)^n \times \Delta \vec{r}_4 + (\vec{r}_1 - \vec{r}_3)^n \times \Delta \vec{r}_2] \\ &\quad + \frac{1}{2} \{ \Delta \vec{r}_2 \times (\Delta \vec{r}_3 - \Delta \vec{r}_1) + \Delta \vec{r}_4 \times (\Delta \vec{r}_1 - \Delta \vec{r}_3) \}. \end{aligned} \quad (3.10)$$

Using Eq. (3.2), where the grid vectors  $\vec{a}_p^{z,*}$  are shown in Fig. 1 ( $\vec{a}_{p=1} = \vec{a}_1 + \vec{a}_8$ , etc.), results in

$$\begin{aligned} \Delta V_z^{\text{cmp}} &\equiv \sum_{p=1}^4 \vec{a}_p^{z,*} \cdot \Delta \vec{r}_p \\ &= \frac{1}{2} [\dots \text{same as above} \dots] + \frac{\alpha}{2} \{ (\Delta \vec{r}_2^* \times \Delta \vec{r}_3 + \Delta \vec{r}_2 \times \Delta \vec{r}_3^*) - (\Delta \vec{r}_2^* \times \Delta \vec{r}_1 + \Delta \vec{r}_2 \times \Delta \vec{r}_1^*) \\ &\quad + (\Delta \vec{r}_4^* \times \Delta \vec{r}_1 + \Delta \vec{r}_4 \times \Delta \vec{r}_1^*) - (\Delta \vec{r}_4^* \times \Delta \vec{r}_3 + \Delta \vec{r}_4 \times \Delta \vec{r}_3^*) \}, \end{aligned} \tag{3.11}$$

where the terms in square brackets are the same in both equations. Thus it is once again seen that if the grid vectors are time-centered ( $\alpha = 1/2$ ), and also for zero force, then these equations and their associated time integrated volumes are identical.

In order to examine the difference in these two volumes further, consider how coordinates are advanced in time. With  $\Delta \vec{r}_p^* = (\vec{v}_p^{n+1,*} + \vec{v}_p^n) \Delta t / 2$  we can write

$$\begin{aligned} \Delta \vec{r}_p^* &= \vec{v}_p^n \Delta t + \vec{F}_p^n (\Delta t)^2 / (2M_p), \\ \Delta \vec{r}_p &= \vec{v}_p^n \Delta t + \vec{F}_p^* (\Delta t)^2 / (2M_p). \end{aligned} \tag{3.12}$$

Now let us pick out the first term in curly brackets in Eq. (3.10) and in Eq. (3.11) that refer to the points 2 and 3 of the quadrilateral in Fig. 1, and subtract these terms with  $\alpha = 1/2$  to obtain

$$\begin{aligned} &[\Delta \vec{r}_2 \times \Delta \vec{r}_3 - \frac{1}{2} (\Delta \vec{r}_2^* \times \Delta \vec{r}_3 + \Delta \vec{r}_2 \times \Delta \vec{r}_3^*)] \\ &= \frac{(\Delta t)^3}{4M} [\vec{v}_2^n \times (\vec{F}_3^* - \vec{F}_3^n) - \vec{v}_3^n \times (\vec{F}_2^* - \vec{F}_2^n)] + \frac{(\Delta t)^4}{4M^2} \left[ \vec{F}_2^* \times \vec{F}_3^* - \frac{1}{2} (\vec{F}_2^n \times \vec{F}_3^* + \vec{F}_2^* \times \vec{F}_3^n) \right]. \end{aligned}$$

This shows that the difference in coordinate and compatible volumes for 2D Cartesian geometry is of order  $(\Delta t)^3$  on a single timestep. When integrating this difference to some global time  $t^n$  one factor of  $\Delta t$  is absorbed into the multiplying constant so that we deduce that the accuracy in time should be of order  $(\Delta t)^2$ .

The preceding arguments justify writing the average error norms defined in Eqs. (3.4), (3.5) in an approximate global form as

$$E_1(t^n) \approx \mathcal{O} \left( \sum_{z=1}^{N_z} (\Delta t)^q \frac{(\Delta x)^r}{V_z} \right) / N_z, \tag{3.13}$$

$$E_{\text{max}}(t^n) \approx \mathcal{O} \left( \max_z (\Delta t)^q \frac{(\Delta x)^r}{V_z} \right). \tag{3.14}$$

In the above expressions, the powers  $q$  and  $r$  denote global orders of accuracy in space and time, respectively; notice that for the max-norm,  $r$  is set to unity in anticipation of the expected result. The zone dimensions may not be even close to uniform, so one may have quite different values of  $\Delta x$  and zone volume  $V_z$  across the grid at any given time. Because of how the truncation error enters in the preceding discussion, the approximate error estimators given in Eq. (3.13) are a product of space and time error, instead of a separate sum of such terms as usually results from a direct Taylor series expansion of a system of PDE's. The operational use of these error estimators requires some further explanation. As will be seen, although they can indicate the relative quality of one or a set of simulations, they do not always yield an unambiguous value for the spatial accuracy  $r$ , and thus require some care in their utilization.

To determine the powers in the error indicators defined above one performs a series of computations for a set of problems with different space and time resolution. Then by comparing the values of a given error norm at the same time for a given computation, one can calculate the values of the power law dependence, the values of  $q$  and  $r$ . There are essentially three different strategies for doing this calculation. First, with spatial resolution fixed, one scales the CFL number down by factors of two (starting with  $\text{CFL} = 0.25$ ) and runs each simulation to the same final time; this freezes any dependence on the spatial factors in our error norms. Second, the  $\Delta t$  factors in this equation can be effectively held fixed by increasing the CFL number by a factor of two (while staying beneath the 0.25 level) and decreasing the grid spacing by a factor of two in the spatial direction

that determines the CFL number. Then one compares the values of Eq. (3.13) for different runs at the same final time; these runs will have executed approximately the same number of time cycles. Third, one can scale the spatial dimensions holding the CFL number fixed. Next we detail what one must consider when implementing these three strategies.

The first of the above strategies is the only one that is straightforward. By fixing the spatial resolution and scaling the CFL number, each time decreasing the CFL number by a factor of two, usually yields decreasing values of Eq. (3.13) on each iteration by two or four indicating a value of  $q$  of one or two, respectively. This is expected from the previous arguments that show that one should obtain either first or second order accuracy in time depending upon whether the grid vectors are placed full-forward or time-centered on the corrector step. The second strategy attempts to eliminate time dependence from our error estimators; however, for most Lagrangian calculations, the timestep varies significantly throughout any run, so what is fixed is the cycle number to reach a final time, and it is assumed that this eliminates the time dependence between runs. One must then carefully consider how the zone volume  $V_z$  changes with the scaled dimensions in order to conclude an order of spatial accuracy  $r$ . For instance, if the zone size decreases as  $(\Delta x)^2$  and  $E_1(t^n)$  remains constant, then one concludes second order spatial accuracy ( $r = 2$ ). Alternatively, if  $E_1(t^n)$  increases by the same factor that is used to decrease  $\Delta x$ , then one would conclude first order accuracy in space ( $r = 1$ ). The third strategy requires the most scrutiny in its use in that changing a spatial dimension may or may not affect timestep; additionally, the timestep may be determined first by one dimension and later by another, as can happen when a center of convergence is approached by a shock front. However, if the scaled dimension does determine the timestep and if the order of accuracy with respect to time is known (usually second order for centered grid vectors), then one can cancel a factor of  $(\Delta t/\Delta x)^2$  in  $E_1(t^n)$  and use the remainder to determine  $r$ . Again, one must carefully consider how  $V_z$  changes with the scaled spatial dimensions.

Before proceeding to the numerical tests, we wish to note that the local spatial accuracy of the type of finite-volume differencing used with Lagrangian hydrodynamics calculations is usually first order, and never higher than second order. This has been demonstrated previously in the appendix of [13] for 2D Cartesian geometry, but applies generally in any number of dimensions. A geometric illustration of this can be seen in 1D by referring to Fig. 2, in which is depicted a simple 1D grid that is uniform but with different zone spacing to the right and left of a central displacement. Such a grid represents a shock wave travelling from right to left with the shock position at the central two zones that are non-uniform. The spatial gradients that are calculated in this simple case are just spatial differences of quantities such as density and velocity centered at zones and points on a uniform grid, and are thus second order accurate for simple two-point differences. Where the grid is non-uniform the accuracy drops to first order, which is the shock position  $S$  in Fig. 2. This simple case often extends quite naturally to 2D and 3D in the case where the velocity field is said to be grid-aligned. Here the velocity difference  $\Delta \vec{v}$  between any two adjacent grid points is parallel (or possibly zero) to the displacement vector between them. Configurations of this type in 2D or in 3D often have approximately uniform grid spacing except near the location of shocks. In these cases one can often operationally observe second order spatial accuracy with respect to the  $E_1$  error indicator. Theoretically, these calculations are still first order in space with respect to any part of the grid that a shock wave has traversed, since a shock acts as an internal boundary condition applied by means of the artificial viscosity with first order spatial accuracy.

While it has been noted that the order of accuracy of Lagrangian calculations is usually low, it is not the case that our error estimators are meant to simply verify the obvious. They may do this to the extent that they verify that runs are reasonable in this regard. However, their most common use (mainly  $E_1(t^n)$ ) is to indicate when numerical problems arise, and to show in more detail how convergence to a solution is reached. Some examples are given in the next section that illustrate these points.

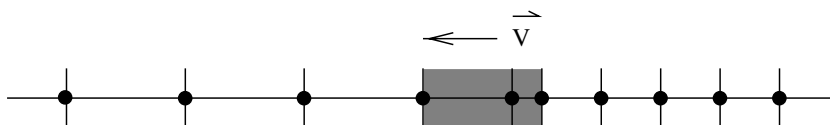


Fig. 2. 1D path of a shock (gray region) travelling from right to left with velocity  $\vec{v}$ . The left part of the domain is unperturbed, whereas the right part has been compressed due to the shock wave.

3.1. Numerical tests

A set of numerical tests are given to validate the error indicators previously defined, and to illustrate how they can be utilized to assess the quality of numerical simulations. These also serve to demonstrate that the size of the entropy error associated with the coordinate and compatible volumes is significant only when severe numerical difficulties, such as numerical instability, arise. The discussion is meant to show that the error estimators are of both a practical and a pedagogical utility. The test problems employed have all been published elsewhere, and thus their setups are not repeated; instead, the previously published results are referenced. Only enough detail is given to make the discussion of the tables given herein intelligible.

Our first example shows how the internal consistency estimator  $E_1(t)$  can be used as a highly sensitive indicator of the development of numerical difficulties during any calculation. For this purpose the Guderley implosion problem is chosen with a resolution of 1000 zones radially and three 30° angles on a 90° quadrant in cylindrical geometry. We use area-weighted differencing to preserve 1D spherical symmetry (see Fig. 3 of [6] for both setup and results), and a CFL number of 0.25. For such resolution this problem has very long-thin zones that eventually develop hourglass difficulties that result in run termination unless subzone pressure forces that counteract this instability are employed [16]. Table 1 gives the cycle number, time, timestep,  $E_1(t)$  norm, and total energy balance for this test case: first, using no stabilizing subzone pressure forces, and then with stabilizing forces and a merit factor of unity. The fact that the calculation has developed numerical difficulties in the first instance can be seen by the sudden increase in  $E_1(t)$  by an order of magnitude, from  $10^{-9}$  to  $10^{-8}$ , between the time of 0.3 and 0.4;  $E_1(t)$  then increases by three additional orders of magnitude at a time of 0.5, and the run terminates with timestep collapse about 1300 cycles later. Notice that the value of total energy balance, given in non-dimensional form in the last column of this table, remains at roundoff error level and that  $E_1(t)$  never reaches a magnitude of order unity. In the second part of Table 1, the results are shown for the case where subzone pressure forces are utilized. This case runs to the final time of 0.8 without any hourglass problems. Although  $E_1(t)$  starts out with a slightly larger value than that of the first run at an earlier time, it shows only a gradual increase as the shock wave travels inward, activating more cells of the grid which can then contribute a non-zero value to  $E_1(t)$ . When the shock wave reflects from the center of convergence just after a time of 0.75, the value of  $E_1(t)$  increases by approximately an order of magnitude, and remains close to constant at the final value shown as the shock wave moves outward. In these runs the grid vectors are time-centered on the corrector step. Therefore, the magnitude of  $E_1(t)$  is small compared to what one would expect the spatial truncation error to be for this grid resolution.

Table 1  
Guderley problem in cylindrical geometry with CFL = 1/4

Cycle	Time $t$	$\Delta t$	$E_1(t)$	Total energy balance
<i>Without anti-hourglass forces</i>				
1709	0.2	1.113E – 4	3.242E – 9	–5.276E – 16
2635	0.3	1.046E – 4	3.835E – 9	5.921E – 17
3627	0.4	0.969E – 4	3.204E – 8	–2.419E – 15
4713	0.5	0.867E – 4	1.187E – 5	–3.612E – 16
6092	0.558	0.97E – 12	8.330E – 4	–1.827E – 15
...	...	Fails	...	...
<i>With anti-hourglass forces</i>				
1708	0.2	1.113E – 4	6.353E – 9	7.912E – 16
2634	0.3	1.046E – 4	7.260E – 9	2.368E – 15
3626	0.4	9.698E – 5	9.221E – 9	2.329E – 15
4710	0.5	8.744E – 5	1.153E – 8	3.106E – 15
⋮	⋮	⋮	⋮	⋮
13,122	0.8	1.515E – 5	5.526E – 5	7.332E – 16

We show results with and without anti-hourglass subzone pressure forces: without these forces the problem fails at time  $t \approx 0.558$ ; with them the problem runs to completion. That the calculation develops numerical difficulties in the first instance is seen by the increase in  $E_1(t)$ . Total energy balance remains at roundoff error level.

In Fig. 3 the log of  $E_1(t)$  versus time is plotted for the cases given in Table 1. The unstable case without anti-hourglass forces increases sharply, and eventually with a large linear slope, indicating exponential growth of the instability after  $t \approx 0.4$ . The stable case shows only linear growth (approximately constant on a semi-log plot), and increases significantly only after shock reflection from the center of convergence, an expected behavior that is due to the wall heating difficulty of all forms of artificial viscosity. Thus the  $E_1(t)$  error norm should be monitored closely for all simulations. Any sudden increase in its value very often indicates a developing numerical problem that is cause for closer scrutiny. Subzone anti-hourglass pressure forces with merit factor,  $M_f = 1$ , are employed in all remaining simulations detailed in this paper.

The next example illustrates how the  $E_1(t)$  error norm varies in both magnitude and in scaling when the grid vectors are time-centered or full-forward on the corrector step, and with varying CFL number between runs. Again the Guderley implosion problem is used with 400 radial zones and three  $30^\circ$  angles. In Table 2 results are given for four different runs. The left side of this table shows the approximate time and number of cycles for CFL numbers 0.25 and 0.125, and the  $E_1(t)$  error norm for the case where the grid vectors are centered at the  $n + \frac{1}{2}$  time level on the corrector step; on the right  $E_1(t)$  is given when the grid vectors are full-forward at the  $n + 1$  time level on the corrector step. Note that there is approximately a three to four order of magnitude increase in the size of  $E_1(t)$  between these two cases. This is expected from the analysis given earlier that showed that for grid vectors placed full-forward, the two definitions of zone volume differ at spatial truncation error level without consideration of any applied forces; the magnitude of  $E_1(t)$  in this case gives an operational measure of spatial truncation error. Also, from the preceding analysis we expect to observe first order scaling in time with grid vectors placed full-forward, and second order accuracy in the time-centered case. Table 2 shows the ratio of the values of  $E_1(t)$  between runs where the CFL number has been halved (cycle number to same final time doubled). One expects a ratio of about two for first order accuracy, and about four for second order accuracy. It is seen that for full-forward grid vectors, this is what is obtained; for grid vectors time-centered, values somewhat larger than four are observed. In general, and with other test problems, one sees this type of behavior as well, usually very close to factors of two or factors of four for these respective grid vector time centerings. The general conclusion is that if the grid vectors are time centered on the corrector step, second order accuracy in time is achieved. It is the spatial accuracy that invariably dominates and determines the quality of the solutions in Lagrangian hydrodynamics calculations. In the remaining simulations,

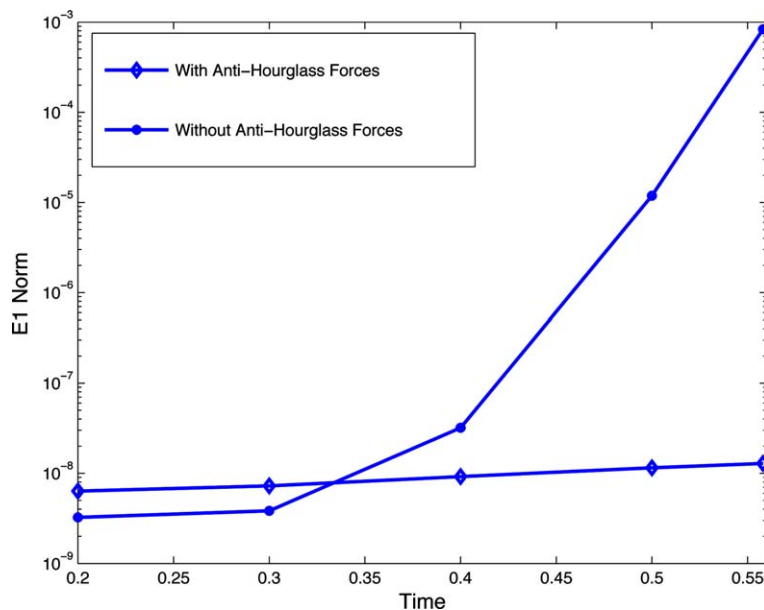


Fig. 3. Semi-log plot of the  $E_1$  norm in time for the Guderley problem in cylindrical geometry (CFL = 1/4). Without anti-hourglass forces, the  $E_1$  norm increases sharply showing exponential growth of the instability after  $t \approx 0.4$ . With anti-hourglass forces, the stable case, growth is linear and a significant increase in  $E_1(t)$  occurs only after shock reflection from the center of convergence.

Table 2  
Guderley problem in cylindrical geometry

CFL	Cycle	Time $t$	Centered grid vectors		Forward grid vectors	
			$E_1(t)$	Ratio	$E_1(t)$	Ratio
1/4	2960	0.7	<b>1.71E – 7</b>	–	1.17E – 3	–
	3433	0.75	3.00E – 6	–	5.13E – 3	–
	5054	0.8	1.01E – 5	–	1.03E – 2	–
1/8	5922	0.7	<b>2.97E – 8</b>	<b>5.75</b>	5.54E – 4	1.37
	6874	0.75	4.73E – 7	6.34	2.55E – 3	2.01
	10087	0.8	1.34E – 6	7.53	5.12E – 3	2.01
				$\geq 4$		$\sim 2$

When the grid vectors are time-centered, the ratios  $E_1(\text{CFL} = 1/4)/E_1(\text{CFL} = 1/8)$  are larger than four (e.g., **Ratio** = **1.71E – 7/2.97E – 8 = 5.75**). Whereas when the grid vectors are full-forward, the ratios are approximately two.

the grid vectors are always time-centered on the corrector step. The data presented throughout this paper constitute a representative sample taken from many simulations.

Before proceeding, we wish to mention that in the context of area-weighted differencing, multiple correctors can and have been used to advance a timestep. In this instance the forces used to compute both  $\Delta \vec{r}_p^*$  and  $\Delta \vec{r}_p$  in Eq. (3.13) are formally at the  $n + \frac{1}{2}$  time level, and we observe a decrease in the values of  $E_1(t)$  by about a factor of two with two correctors over that seen with one time-centered corrector step. The use of more than two correctors does not result in any further decrease in  $E_1(t)$  as roundoff error is always present to seed this error. The use of multiple correctors in this context has not been found to improve the quality of any numerical results and is not recommended.

Our third example contrasts the scaling of the  $E_1(t)$  error norm for the Noh (see [15] for setup) and Guderley problems with time-centered grid vectors but with increasing radial resolution and increasing CFL number so that the number of cycles to run the Guderley problem to the quoted time of 0.74 is about 12,000, and the Noh problem to a time of 0.05 is about 1000. This is an example of the second manner in which  $E_1(t)$  can be utilized, in this case with the dependence on timestep frozen out. Here we attempt to assess the order of spatial accuracy by considering the scaling of the  $E_1(t)$  error norm. In cylindrical geometry the grid is scaled in the radial direction, using 400, 800, and 1600 radial zones, respectively, with three fixed 30° angles. It is seen from Table 3 that the  $E_1(t)$  error norm increases only modestly as the grid is refined radially for the Guderley problem, while it increases by somewhat more than a factor of two for the Noh problem. The Guderley problem is a running shock wave that has not reflected by a time of 0.74, while the Noh problem is a stagnation shock that shows a severe wall heating problem at the center of convergence of the grid. If one looks at the value of the kernel of the error norm  $E_1(t)$  defined for each zone, one finds that as the Noh problem is refined in the radial direction, this error is constant as a function of logical radial index number from the origin. This is a numerical example of non-uniform spatial convergence, and we expect this problem to show only first order spatial accuracy with respect to the  $E_1(t)$  error norm. Thus, if we conclude that the zone volume  $V_z$  in  $E_1(t)$

Table 3  
Guderley and Noh problems in cylindrical geometry

Grid	CFL	Cycle	Time $t$	$E_1(t)$	Ratio
<i>Guderley problem</i>					
400 × 3	1/16	~12,000	0.74	<b>1.90E – 8</b>	<b>1.26</b>
800 × 3	1/8			<b>2.39E – 8</b>	1.39
1600 × 3	1/4			3.32E – 8	–
<i>Noh problem</i>					
400 × 3	1/32	~1000	0.05	3.18E – 7	2.37
800 × 3	1/16			7.53E – 7	2.43
1600 × 3	1/8			1.83E – 6	–

The grid is refined as the CFL increases such that the same number of time steps is performed to reach the final time (12,000 for Guderley problem, 1000 for Noh). Ratios are computed by dividing two consecutive norms.

decreases as the square of the radial zone spacing, then for first order accuracy of the force differencing in the Noh problem ( $r = 1$ ), one expects that  $E_1(t)$  should increase by factors of two as the number of radial zones is successively doubled. Likewise, if the force is effectively calculated with second order spatial accuracy ( $r = 2$ ), then it is expected that  $E_1(t)$  should remain approximately constant. This is close to what is seen for the Guderley problem; these results are given in Table 3. We conclude that this running shock wave problem shows approximate second order spatial accuracy with respect to the  $E_1(t)$  error norm. This is because the zones that contain the shock wave contribute a negligible contribution to  $E_1(t)$  because they are few in number. Order of accuracy is always a function of the norm used to measure it [2].

In the following example we employ the third strategy that was mentioned for utilizing our internal consistency estimators. The Guderley problem is computed in 2D cylindrical geometry with a CFL number of 0.25; the number of radial zones is scaled from 800 to 1600 with three 30° angles. The scaling of both the  $E_1(t)$  and the  $E_{\max}(t)$  norms is examined; these results are given in Table 4. Notice that the number of cycles needed to reach a given time has doubled with an increase in grid size since it is the radial spacing of grid points that determines the timestep for 30° angles before the shock wave intersects the center of convergence. If we make the the same assumption as in the previous example regarding the scaling of the zone size  $V_z$  with the number of radial zones, then the spatial part of the  $E_1(t)$  norm should be close to constant. Thus a factor of approximately four in the ratio of these norms comes from their  $(\Delta t)^2$  time dependence. This reasoning and the results in Table 4 indicate second order accuracy in both space and time. Likewise, the decrease in the  $E_{\max}(t)$  norm by about a factor of two indicates a situation where there is second order accuracy in time but only first order in space, since the growth in the spatial part of this norm cancels one-half of the decrease due to second order time dependence. First order accuracy is what one expects with respect to the  $E_{\max}(t)$  norm. If one locates the position in the grid where the value of the max-norm is achieved, one finds that it tracks the shock location exactly. That is, the value of the kernel that makes up these norms has its maximum at the shock location, and for a given zone, relaxes in magnitude by about a factor of 20 after the shock wave has heated this zone and moved by it. The type of reasoning just employed must be used carefully in that the conclusions depend on both the scaling of  $V_z$  with grid dimensions, and that the timestep is determined by the scaled dimension, which is certainly not always the case.

The Sedov blast wave problem is now considered. The precise setup used is given in [13]; it is run in 2D cylindrical geometry using area-weighted differencing with grids consisting of square zones of size  $45 \times 45$  and  $90 \times 90$ , and with CFL numbers of 0.25 and 0.125. The internal energy is zero in all zones except the single zone at the origin. This zone contains the same total internal energy in all four cases, so the specific internal energy is a factor of eight larger when going from a  $45 \times 45$  to a  $90 \times 90$  grid size. The Sedov problem has always represented a particular challenge for all of the older non-energy-preserving Lagrangian algorithms in that they show a loss of total energy of about 10%. This energy is lost in the first few timesteps and is large enough to raise serious questions about the quality of the solution. For our compatible formulation, total energy conservation is achieved, but the  $E_{\max}(t)$  norm has a relatively high value for these cases. If we consider only the error kernel for the inner zone where all internal energy is initially located, we find that this norm oscillates in time with an approximate period of about 100 cycles and an amplitude of about 1–0.5% and does not rapidly decay. This is a rather large value for this quantity compared to our other cases; however this inner

Table 4  
Guderley problem in cylindrical geometry for CFL = 1/4

Grid	CFL	Cycle	Time $t$	$E_1(t)$	Ratio	$E_{\max}(t)$	Ratio
800 × 3	1/4	5973	0.7	<b>6.13E – 8</b>	–	1.52E – 5	–
		6964	0.75	8.43E – 7	–	2.77E – 4	–
		10,367	0.8	3.60E – 6	–	1.14E – 3	–
1600 × 3	1/4	14,992	0.7	<b>1.15E – 8</b>	<b>5.33</b>	8.74E – 6	1.74
		14,027	0.75	1.92E – 7	4.39	1.44E – 4	1.92
		21,211	0.8	9.28E – 7	3.88	8.41E – 4	1.36
					~4		~2

The results show that when the grid is refined, the ratios of  $E_1$  norms (**Ratio = 6.13E – 8/1.15E – 8 = 5.33**) are near four, whereas they are approximately two for the ratios of the  $E_{\max}$  norms.

zone expands by about a factor of ten in size ( $10^3$  in volume), so interpreting this difference as a measure of local truncation error about this zone is not unreasonable. If we investigate the error kernel of other zones in the grid it is found that they all oscillate in time with an amplitude that decreases with radial location from the origin, but is constant with respect to logical grid index number when the number of initial zones is doubled in each dimension.

The results of this problem for the four cases mentioned are detailed for the  $E_1(t)$  error norm in Table 5. Unlike in the other examples considered, it is seen that this norm does not change as the CFL number is halved for a fixed initial grid size. This appears to be connected to the oscillation of this error at all grid points, something that is not seen in our other calculations. There is a decrease in the  $E_1(t)$  norm by a factor of between two and three when going from  $45 \times 45$  to  $90 \times 90$  zones with the CFL number held fixed. Notice from Table 5 that it also takes about three times the number of cycles in this instance to reach the same final time. So just as for the older Lagrangian algorithms, this problem is still somewhat of an enigma.

The last example that is considered is the Guderley implosion problem in 3D Cartesian geometry. This is run with a spherical initial grid on an octant with three  $30^\circ$  angles in both  $\theta$  and  $\phi$ , and with 100 zones in the radial coordinate with unit initial domain. The relevance of this problem is to show what happens when the symmetry correction factors given in [18] are turned on and off. Corrections to the grid vectors are necessary if a calculation in 3D Cartesian geometry is to preserve 1D spherical symmetry when present in the initial and boundary conditions, as is true for this case. The results from two simulations that are identical except for this symmetry correction procedure are given in Table 6. There it is seen that the magnitude of the  $E_1(t)$  norm is about three to four orders larger for the case where the symmetry corrections are not utilized. With symmetry corrections off, the flow field deviates from being 1D spherical, the velocity vectors are no longer grid-aligned, and the grid distorts in space. This can be seen from the grid and density contours shown in Fig. 4.

Table 5  
Sedov problem in cylindrical geometry

Grid	CFL	Cycle	Time $t$	$E_1(t)$	Ratio CFL	Ratio grid
$45 \times 45$	1/4	369	0.5	$5.60E - 5$	–	–
		551	1.0	$7.38E - 5$	–	–
$45 \times 45$	1/8	677	0.5	$5.43E - 5$	1.03	–
		996	1.0	<b><math>6.80E - 5</math></b>	1.09	–
$90 \times 90$	1/4	1031	0.5	$2.23E - 5$	–	2.51
		1590	1.0	$2.56E - 5$	–	2.88
$90 \times 90$	1/8	1846	0.5	$2.07E - 5$	1.08	2.62
		2843	1.0	<b><math>2.37E - 5</math></b>	1.08	<b>2.87</b>

Ratio CFL (Grid) is the ratio between the  $E_1$  norms obtained for the same grid (CFL number) at the same time but for two different CFL numbers (grids). Notice that Ratio CFL is approximately one and does not improve.

Table 6  
Guderley problem in 3D Cartesian geometry for CFL = 1/4

Cycle	Time $t$	$\Delta t$	$E_1(t)$	Total energy balance
<i>With symmetry corrections</i>				
297	0.30	$1.012E - 3$	$2.757E - 7$	$-3.257E - 15$
636	0.60	$7.386E - 4$	$7.645E - 7$	$-4.312E - 15$
897	0.75	$0.510E - 4$	$1.215E - 5$	$-4.332E - 15$
<i>Without symmetry corrections</i>				
299	0.30	$1.000E - 3$	$8.839E - 4$	$-4.764E - 16$
666	0.60	$0.521E - 3$	$2.313E - 3$	$-9.746E - 16$
1044	0.75	$0.574E - 4$	$1.960E - 2$	$3.726E - 15$

Although total energy is conserved to round-off error, the  $E_1$  norm shows relatively large values when no symmetry corrections are applied; these numbers reflect the fact that 1D symmetry is broken, as seen in Fig. 4.

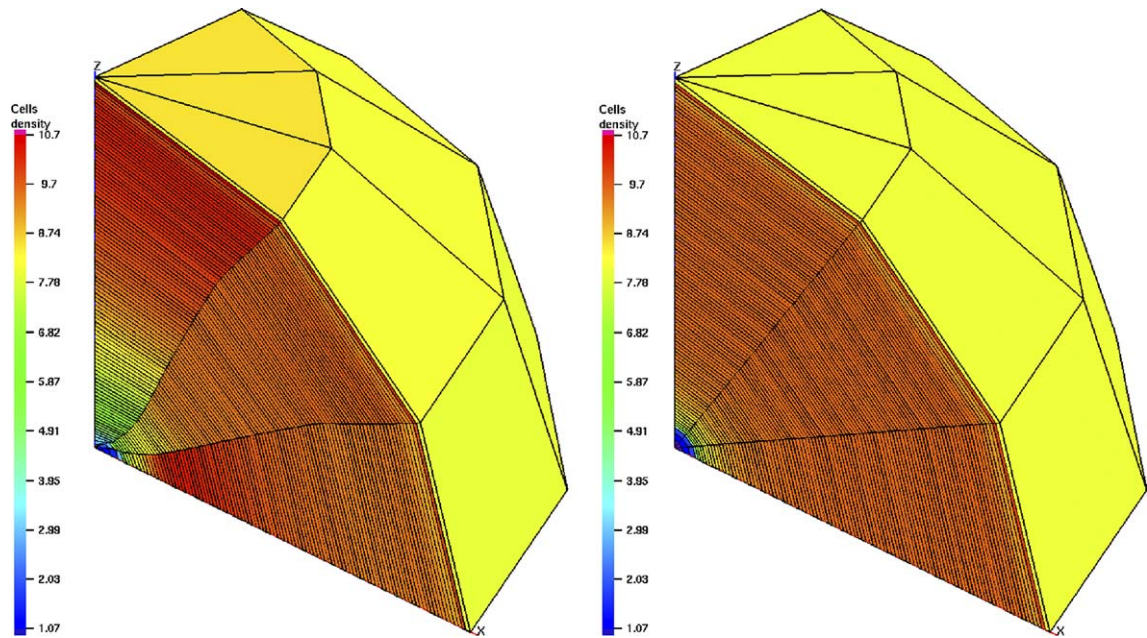


Fig. 4. 3D Guderley problem at  $t = 0.75$  in Cartesian geometry. The mesh is  $100 \times 3 \times 3$  on an octant of the unit sphere. Grid and density contours are shown. Left: 1044 time steps with symmetry corrections off (the loss of 1D symmetry is quantified in Table 6 where the  $E_1$  norm is of truncation error size). Right: 897 time steps with symmetry corrections on.

The lack of 1D symmetry preservation in 3D Cartesian geometry with an initially spherical grid is not a numerical instability, as was the hourglassing case of our first example. This is seen by the fact that although the  $E_1(t)$  norm is about three to four orders of magnitude larger with symmetry corrections off, compared to the case with them on, these norms scale with time in the same manner. These calculations illustrate the ability of the internal consistency error norms to detect numerical problems of differing origins with respect to any given simulation.

#### 4. Numerical stability

For any computational algorithm to be useful it must be numerically stable. By numerical stability one means that if the underlying set of continuum of equations is stable, which says that the continuum system has no growing solutions, then the differenced form of this system should also contain no growing solutions. This is a necessary condition for a useful numerical algorithm. If the underlying continuum system of equations has energy source terms that allow growing solutions, then these terms are omitted from the stability analysis. That is, a numerical stability analysis only makes sense for a continuum system of equations that is already stable. For terms that produce growth of a solution one is only interested in the numerical accuracy with which these terms are differenced. Often very simple subsystems of equations yield the correct numerical stability results for much more complex ones; however, the selection of a proper subsystem can be a bit of an art form. In our case, the simple second order wave equation in one space dimension, written as two coupled first order equations, is utilized for this purpose. These equations are discretized in the next subsection, and the stability of the two-step predictor–corrector scheme described earlier is analyzed using Fourier analysis [2]. The results reveal a stability diagram for constant space step and time step that has not been given previously.

It is difficult to empirically observe a precise stability boundary for a Lagrangian hydrodynamics algorithm because such calculations are typically run with a constant CFL number, but with a grid spacing and a time-step that can vary greatly during a simulation. Also, the definition of the scale length used in computing the CFL number with respect to non-uniform zones is not unique. In order to verify the results of the stability analysis derived using Fourier analysis of our simple system of equations, a numerical test problem is

constructed that eliminates the above noted difficulties. This test problem is then used to substantiate the analytical results for the full system of equations in all three spatial dimensions.

#### 4.1. Stability utilizing the 1D second order wave equation

The 1D second order wave equation written as a coupled first order system with unit velocity is given by

$$\frac{\partial u}{\partial t} = \frac{\partial v}{\partial x}, \quad \frac{\partial v}{\partial t} = \frac{\partial u}{\partial x}, \tag{4.1}$$

where  $u = u(x, t)$  can be thought of as the velocity, so that the first equation is that for momentum, and  $v = v(x, t)$  is the pressure or density in the more general system given by Eqs. (2.1), (2.2). Note that in our simplified model there is no equation of state (EOS), so that if this model yields meaningful results we expect these results to be independent of the form of the EOS of the more general equations.

On a 1D domain  $\Omega = [x_{\min}, x_{\max}]$ , a mesh is defined by  $N_z$  zones/cells and  $N_p = N_z + 1$  points such that  $x_j = x_{\min} + (j - 1)\Delta x$  where  $\Delta x = x_{j+1} - x_j$  is the size of a cell  $j + \frac{1}{2}$ . Time is discretized using a time step  $\Delta t = t^{n+1} - t^n$  and we define the CFL number as  $r \equiv \Delta t / \Delta x$ . For our stability analysis, we assume that  $\Delta x$  and  $\Delta t$  are constant in time. The velocity  $u$  is discretized on node  $j$  at time  $t^n = n\Delta t$  as  $u_j^n$ , whereas  $v$  is placed at the center of the cell  $j + \frac{1}{2}$  as  $v_{j+\frac{1}{2}}^n$ . The numerical scheme is denoted by  $S_\alpha$ , where  $0 \leq \alpha \leq 1$ , and is defined by the following equations

- *Predictor step:*  $u_j^*$ ,  $v_{j+1}^*$  at time  $t^n + \Delta t$ ;  $\bar{v}_{j+\frac{1}{2}}^*$  at time  $t^n + \alpha\Delta t$

$$u_j^* = u_j^n + r(v_{j+\frac{1}{2}}^n - v_{j-\frac{1}{2}}^n), \tag{4.2}$$

$$v_{j+\frac{1}{2}}^* = v_{j+\frac{1}{2}}^n + r\left(\frac{1}{2}(u_{j+1}^* + u_{j+1}^n) - \frac{1}{2}(u_j^* + u_j^n)\right), \tag{4.3}$$

$$\bar{v}_{j+\frac{1}{2}}^* = \alpha v_{j+\frac{1}{2}}^* + (1 - \alpha)v_{j+\frac{1}{2}}^n. \tag{4.4}$$

- *Corrector step:* uses the \* values to increment  $u^n$  and  $v^n$

$$u_j^{n+1} = u_j^n + r(\bar{v}_{j+\frac{1}{2}}^* - \bar{v}_{j-\frac{1}{2}}^*), \tag{4.5}$$

$$v_{j+\frac{1}{2}}^{n+1} = v_{j+\frac{1}{2}}^n + r\left(\frac{1}{2}(u_{j+1}^{n+1} + u_{j+1}^n) - \frac{1}{2}(u_j^{n+1} + u_j^n)\right). \tag{4.6}$$

This is a two parameter system: the CFL number  $r$ , and the parameter  $\alpha$  that time-averages the pressure from the predictor step to the momentum equation on the corrector step. With  $\alpha = 0$  the predictor and corrector steps are the same and the scheme is known to be unconditionally unstable. A few additional remarks on this discretization are in order; first, in the equations used to advance  $v_{j+1/2}^*$  and  $v_{j+1/2}^{n+1}$  in time, an average of the values of  $u$  at the advanced and old time levels is used on the RHS of Eqs. (4.3), (4.6) instead of a full-forward value. This is due to the fact that in the equations that are actually solved numerically, Eq. (2.2), also uses an average of old and advanced velocity to form the displacement  $\Delta \vec{r}_p$ . This time centering is necessary if we expect the simple model to accurately represent the compatible hydrodynamics equations that we wish to solve. The time centering parameter  $\alpha$  in the corrector step, that is used in Eq. (4.5), has two important values:  $\alpha = 1/2$  is referred to as time-centered, and  $\alpha = 1$  is referred to as full-forward.

By substituting Eqs. (4.2)–(4.4) into (4.5) and (4.6) we obtain explicit formulas for  $u$  and  $v$  at time  $t^{n+1}$ :

$$u_j^{n+1} = u_j^n + r(v_{j+\frac{1}{2}}^n - v_{j-\frac{1}{2}}^n) + \alpha r^2(u_{j+1}^n - 2u_j^n + u_{j-1}^n) + \frac{1}{2}\alpha r^3(v_{j+\frac{3}{2}}^n - 3v_{j+\frac{1}{2}}^n + 3v_{j-\frac{1}{2}}^n - v_{j-\frac{3}{2}}^n), \tag{4.7}$$

$$v_{j+\frac{1}{2}}^{n+1} = v_{j+\frac{1}{2}}^n + r(u_{j+1}^n + u_j^n) + \frac{1}{2}r^2(v_{j+\frac{3}{2}}^n - 2v_{j+\frac{1}{2}}^n + v_{j-\frac{1}{2}}^n) + \frac{1}{2}\alpha r^3(u_{j+2}^n - 3u_{j+1}^n + 3u_j^n - u_{j-1}^n) + \frac{1}{4}\alpha r^4(v_{j+\frac{5}{2}}^n - 4v_{j+\frac{3}{2}}^n + 6v_{j+\frac{1}{2}}^n - 4v_{j-\frac{1}{2}}^n + v_{j-\frac{3}{2}}^n). \tag{4.8}$$

A convenient way to analyze such schemes, and which is due to Von Neumann [2], is to assume a solution of the form:  $u^n = u^0 \lambda^n e^{i\theta j \Delta x}$  and  $v_{j+\frac{1}{2}}^n = v^0 \lambda^n e^{i\theta(j+\frac{1}{2})\Delta x}$  where  $\theta$  is a real parameter, and  $i = \sqrt{-1}$ . The quantity  $\lambda = \lambda(\theta)$  is determined by substituting these forms into Eqs. (4.7) and (4.8). After some algebraic manipulation, these equations can be written as the linear system

$$\mathbf{M} \begin{pmatrix} u^0 \\ v^0 \end{pmatrix} \equiv \begin{pmatrix} \lambda + A & iC \\ iC & \lambda + B \end{pmatrix} \begin{pmatrix} u^0 \\ v^0 \end{pmatrix} = \begin{pmatrix} 0 \\ 0 \end{pmatrix}, \tag{4.9}$$

where  $A, B, C$  are defined by

$$A = -1 + 4\alpha r^2 s^2, \quad B = -1 + 2r^2 s^2 (1 - 2\alpha r^2 s^2), \quad C = 2rs(1 - 2\alpha r^2 s^2)$$

and  $s = \sin(\theta/2)$ . If this system is to be solved for any vector  $(u^0, v^0)$ , the determinant of the matrix  $\mathbf{M}$  must be zero, that is,  $\det(\mathbf{M}) = \lambda^2 + \lambda(A + B) + AB - C^2 = 0$ . Thus,  $\det(\mathbf{M})$  is a polynomial in  $\lambda$ , the complex roots of which are

$$\lambda^\pm = -\frac{A+B}{2} \pm \sqrt{\frac{(A-B)^2}{4} + C^2}. \tag{4.10}$$

For numerical stability the solution vector must not increase in magnitude with time, or  $|(u^{n+1}, v^{n+1})| \leq |(u^n, v^n)|$ , must hold. Thus we require that  $|\lambda^\pm| \leq 1$ . Our objective is to characterize the maximum value of the CFL number  $r$  such that, given a particular value of  $\alpha$ ,  $|\lambda^\pm| \leq 1$ .

$\lambda^\pm \in \mathbb{C}$ : In this case  $\frac{(A-B)^2}{4} + C^2 < 0$ , and we can instead consider

$$|\lambda^\pm|^2 = \left(\frac{A+B}{2}\right)^2 - \frac{(A-B)^2}{4} - C^2 = \frac{AB}{2} - C^2 = 1 - 2(2\alpha - 1)r^2 s^2 - 4\alpha r^4 s^4.$$

Two cases must be considered:

- if  $\alpha < 1/2$ , then  $-2(2\alpha - 1)r^2 s^2 > 0$  and there exists  $r$  small enough such that  $-2(2\alpha - 1)r^2 s^2 > 4\alpha r^4 s^4$  for any  $s$  leading to  $|\lambda^\pm|^2 > 1$ ; the scheme  $\mathbf{S}_{\alpha < 1/2}$  is therefore unconditionally unstable;
- if  $\alpha \geq 1/2$ , then  $-2(2\alpha - 1)r^2 s^2 - 4\alpha r^4 s^4 \leq 0$  for any  $s$  resulting in  $|\lambda^\pm|^2 \leq 1$  independent of  $r$ .

$\lambda^\pm \in \mathbb{R}$ : In this case  $\frac{(A-B)^2}{4} + C^2 \geq 0$ , and we need only to focus on the case  $\alpha \geq 1/2$ , as the case  $\alpha < 1/2$  has just been shown to be unconditionally unstable (see above). Several examples are depicted in Fig. 5, where the discriminant (thick line) and  $\lambda^\pm \in \mathbb{R}$  (thin lines) are plotted. These plots show for which  $\theta$  the discriminant is positive. Moreover, for stability we need  $-1 \leq \lambda^\pm \leq 1$ . It can easily be shown that the maximum value of  $|\lambda^\pm|$  is always reached for the largest wave number  $\theta = \pm\pi$ . Therefore, we compute the eigenvalues when  $s = \sin(\frac{\theta}{2}) = 1$ .

- $\alpha = 1$ : the eigenvalues are given by (see Fig. 6 left curve)

$$\lambda^\pm = 1 - r^2(3 - 2r^2) \pm r\sqrt{-4 + 17r^2 - 12r^4 + 4r^6},$$

using  $r = 1$ , we obtain  $|\lambda^\pm| = |\pm\sqrt{5}| > 1$ . The scheme is unstable in this case. On this other hand, choosing the value  $r = 1/\sqrt{2} = 1/\sqrt{2\alpha}$  yields  $|\lambda^\pm| = 1$ . (In fact, if  $r > 1/\sqrt{2}$ , then  $|\lambda^\pm| > 1$  resulting in instability.) Therefore, for  $\alpha = 1$  and  $\lambda^\pm \in \mathbb{R}$  one expects stability for the CFL condition:  $r \leq 1/\sqrt{2}$ .

- $\alpha = 3/4$ : the eigenvalues are given by (see Fig. 6 middle curve)

$$\lambda^\pm = 1 - \frac{r^2}{2}(5 - 3r^2) \pm \frac{r}{2}\sqrt{-16 + 49r^2 - 30r^4 + 9r^6},$$

which is exactly equal to  $\pm 1$  if  $r = 1/\sqrt{2/3} = 1/\sqrt{2\alpha}$ . (Again if  $r > 1/\sqrt{2/3}$ , then  $|\lambda^\pm| > 1$ .) Therefore, for  $\alpha = 3/4$  and  $\lambda^\pm \in \mathbb{R}$  one expects stability for the CFL condition:  $r \leq 1/\sqrt{2/3}$ .

- $\alpha = 1/2$ : the eigenvalues are given by (see Fig. 6 right curve)

$$\lambda^\pm = 1 - r^2(2 - r^2) \pm r\sqrt{-4 + 8r^2 - 4r^4 + r^6},$$

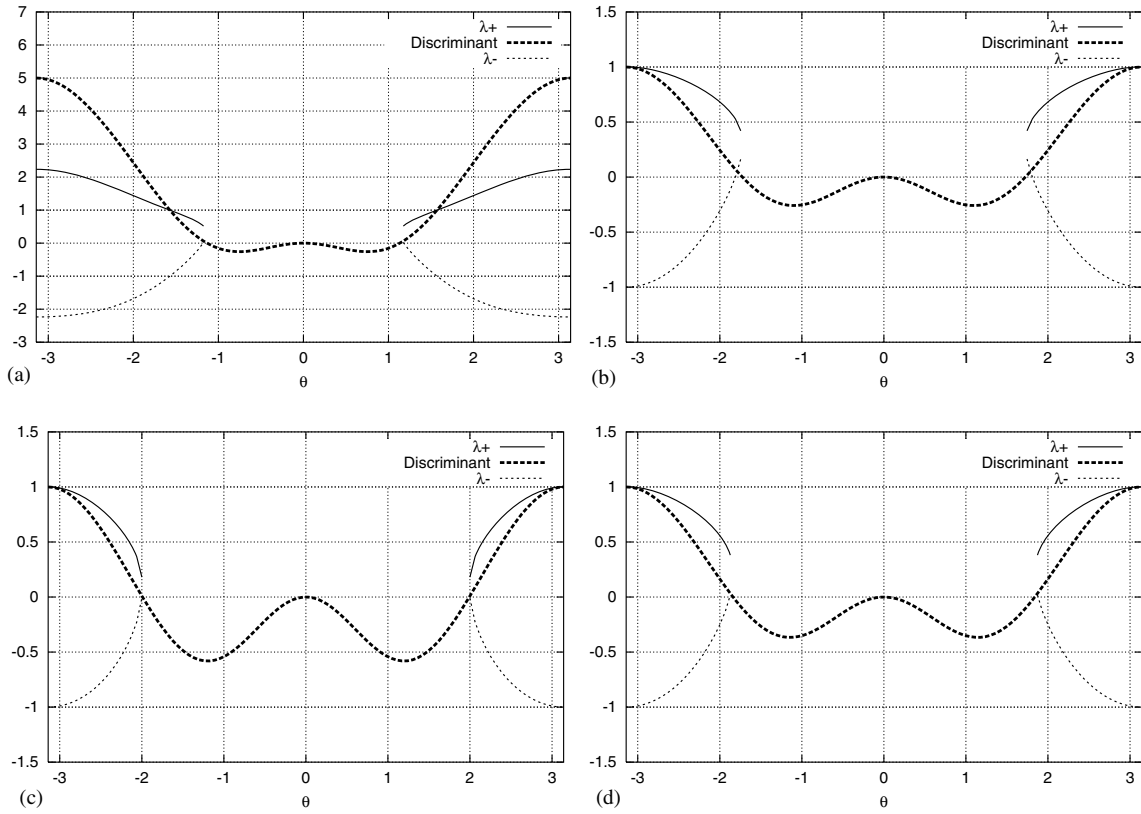


Fig. 5. Discriminant (thick dashed line) and real eigenvalues  $\lambda^\pm$  (thin lines) as a function of  $\theta \in [-\pi, \pi]$ . (a) If  $\alpha = 1$  and  $r = 1$ , then there exist  $\theta \in [-\pi, \pi]$  such that  $|\lambda^\pm| > 1$ . (b) If  $\alpha = 1$  and  $r = 1/\sqrt{2\alpha}$ , then  $|\lambda^\pm| \leq 1$ . (c) If  $\alpha = 1/2$  and  $r = 1$ , then  $|\lambda^\pm| \leq 1$ . (d) If  $\alpha = 3/4$  and  $r = 1/\sqrt{2\alpha}$ , then  $|\lambda^\pm| \leq 1$ .

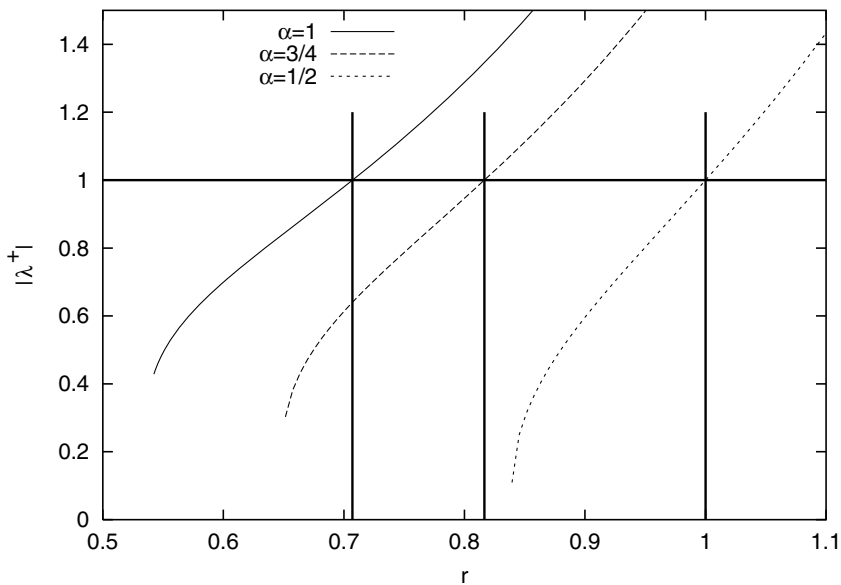


Fig. 6.  $|\lambda^+|$  as a function of  $r$  for  $\lambda^+ \in \mathbb{R}$ . For stability  $|\lambda^+|$  must be less than 1 (thick horizontal line). For which  $r_{\max}$  (vertical dashed line) do we have  $\lambda^+ = 1$ ? Left curve: for  $\alpha = 1$ ,  $r_{\max} = 1/\sqrt{2}$ . Middle curve: for  $\alpha = 3/4$ ,  $r_{\max} = 1/\sqrt{2} \cdot 3/4$ . Right curve: for  $\alpha = 1/2$ ,  $r_{\max} = 1/\sqrt{2} \cdot 1/2 = 1$ .

which is exactly equal to  $\pm 1$  if  $r = 1 = 1/\sqrt{2\alpha}$ . (As is now expected, if  $r > 1$ , then  $|\lambda^\pm| > 1$ , which results in numerical instability.) Therefore, for  $\alpha = 1/2$  and  $\lambda^\pm \in \mathbb{R}$  one expects stability for the classical CFL condition:  $r \leq 1$ .

In summary, the schemes  $S_\alpha$  are unconditionally unstable if  $\alpha < 1/2$ , and stable if  $\alpha \geq 1/2$  and if the CFL condition  $r \leq 1/\sqrt{2\alpha}$  is obeyed (see Fig. 7). Typically, a CFL number less than the maximum allowed for stability is used, most commonly the CFL number  $r = 1/4$ . In Fig. 8,  $|\lambda^+|$  (for three schemes  $\alpha = 1, \frac{3}{4}, \frac{1}{2}$ ) is plotted

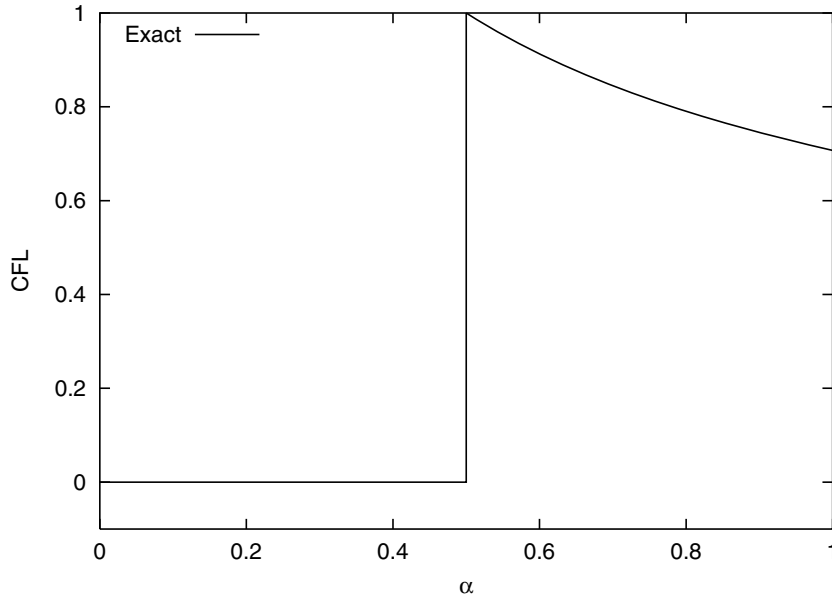


Fig. 7. CFL condition as a function of  $\alpha$  for the family of schemes  $S_\alpha$ . The schemes  $S_\alpha$  are unconditionally unstable for  $\alpha < 1/2$ ; stable for  $\alpha \geq 1/2$  and with CFL condition  $r \leq 1/\sqrt{2\alpha}$ .

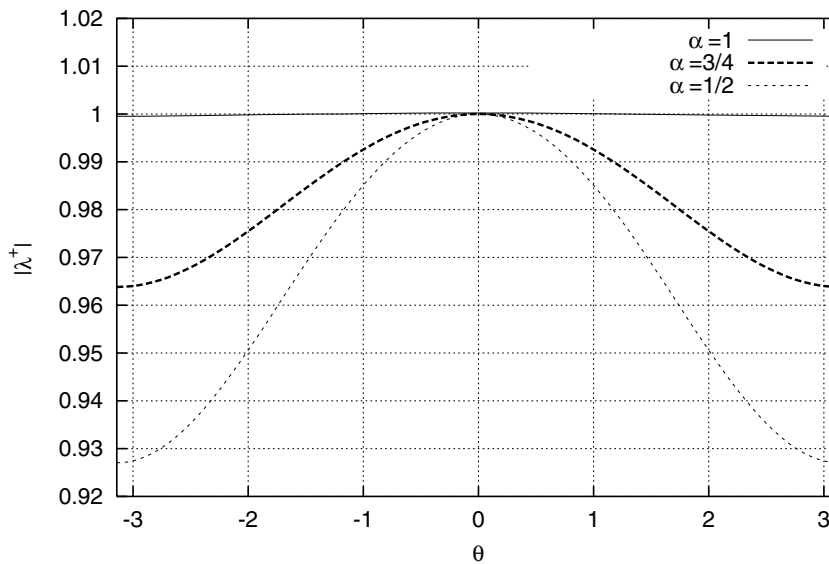


Fig. 8. Dissipation of the schemes  $S_1, S_{\frac{3}{4}}, S_{\frac{1}{2}}$  for a fixed CFL number  $r = 1/4$ .  $|\lambda^+|$  is plotted as a function of  $\theta \in [-\pi, \pi]$ . ( $\alpha = 1, \frac{3}{4}, \frac{1}{2}$  are denoted by straight, thick dashed, dashed lines, respectively).

as a function of  $\theta \in [-\pi, \pi]$  for the fixed CFL number  $r = \frac{1}{4}$ . This plot shows that the scheme defined by  $\alpha = 1/2$ , which lies on the stability boundary, is the least dissipative of the family  $\alpha \geq 1/2$ . The full-forward scheme  $S_1$  damps more than any other.

#### 4.2. Stability of the compatible hydrodynamics equations

The previous stability analysis has been performed for the 1D coupled system of wave equations using a discretization that, although simplified, does indeed correspond to that utilized for the more general system. In order to verify that these results are valid in the more general case, the full compatible hydrodynamic system of equations are solved for the following model problem. Consider the fluid equations in 1D, 2D, and 3D Cartesian geometry with the initial conditions: uniform density  $\rho = 1$ , ideal gas law EOS with  $\gamma = 5/3$ , a sound speed of  $c_s = 1$ , and velocity  $\vec{v} = 0$ . A unit domain with uniform zone size is constructed:  $10$ ,  $10^2$ ,  $10^3$  zones typically, but we also use slightly larger values to rule out surface effects since reflective boundary conditions are imposed on all faces of the domain. In 1D only, the pressure is seeded with a random perturbation at the  $10^{-15}$  level whenever the EOS is called; in 2D and in 3D, the roundoff error that automatically occurs when calculating the grid vectors that are used to construct the corner force for each predictor and corrector stage of a timestep is sufficient to seed numerical instability (in 1D Cartesian geometry these are fixed at unity). Since for this problem no velocity should develop, simulations are run for a very large number of time cycles, typically  $10^5$ , and with varying values for the CFL number  $r$ , and time-centering parameter  $\alpha$ , in the corrector step. A sensitive gauge that provides a useful way to monitor the stability of any given simulation is to track the total kinetic energy  $K^{\text{CFL}}(t^n) \equiv \frac{1}{2} \sum_p M_p (\vec{v}_p^n)^2$ . Since the density and domain size are scaled to unity, this number should remain at the square of machine precision, about  $10^{-28}$ – $10^{-30}$  in our case. For an unstable scheme it is observed that  $K^{\text{CFL}}(t^n)$  grows by several orders of magnitude long before the  $10^5$  cycle limit is reached. Using this test one can very accurately scope out the stability boundary in  $r$  and  $\alpha$  space for all three dimensions. The 1D results are found to exactly match those produced by our analysis of the simplified 1D system of equations (4.1) (see Fig. 7); the 2D and 3D results are also found to be identical to those of the simplified 1D system of equations. Thus we conclude that the stability analysis performed on the 1D simplified system of equations is valid for the full hydrodynamic equations in all spatial dimensions. Although the artificial viscosity is turned off in this test problem, this term acts only as an addition to the pressure as far as stability is concerned. This point is stressed in the original paper that introduced this concept [4]. We also note that the same stability diagram (Fig. 7) is obtained for this test problem using an isothermal EOS, and further supports our conclusion that the numerical stability of the compatible Lagrangian hydrodynamics equations is EOS independent.

## 5. Conclusions

The theme of this paper is to clarify numerical issues concerning the internal consistency, stability, and accuracy of a recent discretization of the equations of fluid dynamics cast into Lagrangian form that we refer to as the discrete, compatible formulation. The proper resolution of the issues mentioned are central to the understanding of any numerical algorithm. Although Lagrangian hydrodynamics algorithms are very old, they languished until recently as attention in computational fluid dynamics turned to broader areas and domains of interest. The central feature of this more modern form of Lagrangian hydrodynamics is its ability to exactly conserve mass, momentum, and total energy without the need to use these quantities directly as dependent variables. It instead retains density, velocity, and specific internal energy as dependent variables as did the earlier version of this algorithm; these variables are more appropriate to compressible high speed flow calculations.

The internal consistency of this algorithm was investigated by analyzing the difference between the two definitions of zone volume that it utilizes. This difference comes about because of the subtle relationship of surface area to volume that characterizes any closed volume, and thus is seen to arise quite generally and naturally. It was shown that this difference can be used to ascertain many properties of a simulation, and thus has direct and practical significance. Non-dimensional internal consistency norms were constructed based on the difference in these two volumes. These can be used to operationally measure the non-dimensional

magnitude of the truncation error of a calculation by placing the grid vectors from which the corner force is calculated at the fully advanced time level on the corrector step. The accuracy in both space and time can also be measured, and results were found to correspond to the first or second order accuracy that one expects in space or time with the type of finite-volume differencing employed with Lagrangian schemes. It was also shown that some care must be exercised in the use and interpretation of these norms/estimators. More importantly, the difference in these two definitions of zone volume, which can be interpreted as a form of entropy error, was demonstrated to be significant only when numerical instability occurs, or other numerical difficulties, such as a loss of lower dimensional symmetry, appear. A precipitous increase in this quantity during any calculation is a sensitive indication of the development of numerical difficulties. Otherwise this difference remains at or far below truncation error levels. A numerical stability analysis of the two level predictor/corrector time integration scheme employed was also performed: first with a simplified set of model equations using standard Fourier stability analysis, and then using a properly constructed test problem that verifies this analysis for the actual system of equations in all three spatial dimensions. This stability analysis showed that our compatible system of equations with predictor–corrector time integration is stable for CFL number  $r \leq 1/\sqrt{2\alpha}$  and  $\alpha \geq 0.5$ , where  $\alpha$  is the time centering parameter of the pressure on the corrector step; otherwise, it is unconditionally unstable.

The principal conclusion of this study is that the corner force, which is the central feature of this numerical scheme, should be placed at the time-centered  $n + \frac{1}{2}$  time level on the corrector step of a cycle. This centering should be performed with respect to both the grid vectors, to minimize the difference in the two zone volumes used in this formulation, and with respect to the total stress (pressure plus deviators, and artificial stresses such as viscosity and anti-hourglass forces). Corner force time-centering results in the least amount of numerical dissipation and the largest stability margin. However, this is also seen to be just at the stability boundary, and is thus a somewhat different choice than is often made with numerical schemes (particularly ODE solvers) where the timestep is chosen from within the stability region.

## Acknowledgments

We wish to acknowledge useful discussions with B. Wendroff concerning the stability analysis of the predictor/corrector time integration scheme: specifically, to have correctly conjectured the  $1/\sqrt{2\alpha}$  stability bound. This work was supported by the Advanced Strategic Computing Initiative (ASCI) of the US Department of Energy.

## References

- [1] H.A. Bethe, R. Christy, R.R. Davis, R.P. Feynman, S. Frankel, E.J. Konopinski, N. Livesay, N. Metropolis, E. Nelson, IBM calculations of implosion hydrodynamics, Los Alamos National Laboratory report, LA-94, June 20, 1944, unclassified, cover only.
- [2] R.D. Richtmyer, K.W. Morton, *Difference Methods for Initial-Value Problems*, second ed., Interscience, New York, 1967 (Chapter 12).
- [3] B. Alder, S. Fernbach, M. Rotenberg (Eds.), *Methods in Computational Physics*, vol. 3, 1964, various articles.
- [4] J. VonNeumann, R.D. Richtmyer, A method for the calculation of hydrodynamic shocks, *J. Appl. Phys.* 21 (1950) 232–237.
- [5] W.B. Goad, WAT: a numerical method for two-dimensional unsteady fluid flow, Los Alamos National Laboratory Report, LAMS-2365, 1960.
- [6] E.J. Caramana, P.P. Whalen, Numerical preservation of symmetry properties of continuum problems, *J. Comput. Phys.* 141 (1998) 174–198.
- [7] A.P. Favorskii, Variational-discrete models of hydrodynamics equations, *Diff. Equations* 16 (1980) 1308–1321.
- [8] L.G. Margolin, T.F. Adams, *Spatial differencing for finite difference codes*, Los Alamos National Laboratory Report, LA-10249, 1985.
- [9] A.A. Samarskii, V.F. Tishkin, A.P. Favorskii, M.J. Shashkov, Operational finite difference schemes, *Diff. Equations* 17 (1981) 854–862.
- [10] L.G. Margolin, A.E. Tarwater, A diffusion operator for Lagrangian meshes, Lawrence Livermore National Laboratory Report, UCRL-95652, 1986.
- [11] D.E. Burton, Exact conservation of energy and momentum in staggered-grid hydrodynamics with arbitrary connectivity, *Advances in the Free-Lagrange Method*, Springer, New York, 1990.
- [12] D.E. Burton, Multidimensional discretizations of conservation laws for unstructured polyhedral grids, Lawrence Livermore National Laboratory Report, UCRL-JC-118306, 1994.

- [13] E.J. Caramana, D.E. Burton, M.J. Shashkov, P.P. Whalen, The construction of compatible hydrodynamics algorithms utilizing conservation of total energy, *J. Comput. Phys.* 146 (1998) 227–262.
- [14] R. Loubère, E.J. Caramana, The force/work differencing of exceptional points in the discrete, compatible formulation of Lagrangian hydrodynamics, LAUR-04-8906, *J. Comput. Phys.*, in press, doi:10.1016/j.jcp.2005.11.022.
- [15] E.J. Caramana, M.J. Shashkov, P.P. Whalen, Formulations of artificial viscosity for multi-dimensional shock wave computations, *J. Comput. Phys.* 144 (1998) 70–97.
- [16] E.J. Caramana, M.J. Shashkov, Elimination of artificial grid distortion and Hourglass-type motions by means of Lagrangian subzonal masses and pressures, *J. Comput. Phys.* 142 (1998) 521–561.
- [17] E.J. Caramana, R. Loubère, Curl-q: a vorticity damping artificial viscosity for Lagrangian hydrodynamics calculations, LAUR-05-6618, *J. Comput. Phys.* 215 (2006) 385–391.
- [18] E.J. Caramana, C.L. Rousculp, D.E. Burton, A compatible, energy and symmetry preserving Lagrangian hydrodynamics algorithm in three-dimensional Cartesian geometry, *J. Comput. Phys.* 157 (2000) 89–119.